

Enhancing vibrational light-matter coupling strength beyond the molecular concentration limit using plasmonic arrays

Manuel Hertzog,[†] Battulga Munkhbat,[‡] Denis G. Baranov,[‡] Timur O. Shegai,^{*,‡}
and Karl Börjesson^{*,†}

[†]*Department of Chemistry and Molecular Biology, University of Gothenburg, Kemigården 4, 412 96, Gothenburg, Sweden*

[‡]*Department of Physics, Chalmers University of Technology, 412 96, Gothenburg, Sweden*

E-mail: timurs@chalmers.se; karl.borjesson@gu.se

Abstract

Vibrational strong coupling is emerging as a promising tool to modify molecular properties, by making use of hybrid light-matter states known as polaritons. Fabry-Pérot cavities filled with organic molecules are typically used, and the molecular concentration limits the maximum reachable coupling strength. Developing methods to increase the coupling strength beyond the molecular concentration limit are highly desirable. In this letter, we investigate the effect of adding a gold nanorod array into a cavity containing pure organic molecules, using FT-IR microscopy and numerical modeling. Incorporation of the plasmonic nanorod array, that acts as artificial molecules, leads to an order of magnitude increase in the total coupling strength for the cavity filled with organic molecules. Additionally, we observe a significant narrowing of the plasmon linewidth inside the cavity. We anticipate that these results will be a step forward in exploring vibropolaritonic chemistry and may be used in plasmon based bio-sensors.

Keywords

Vibropolariton, Strong coupling, Plasmonic, Polaritonic chemistry

Introduction

Strong light-matter coupling has attracted considerable attention in the past couple of years due to the potential applications it offers in physical and chemical sciences.¹⁻⁴ For example, strong coupling of organic molecules has been shown to modify the rate of a photoisomerization reaction,^{5,6} increase electronic transport,⁷ and expand the length scale of Förster energy transfer.⁸⁻¹⁰ Not to mention other effects of strong coupling such as selective manipulation of excited states,¹¹ suppression of photo-oxidation¹² or reducing photodegradation in polymers.¹³ Recently, vibrational strong coupling has come into focus as a promising physical tool to control molecular properties. Since the first experimental evidences of vibrational strong coupling (VSC) in both solid¹⁴⁻¹⁶ and liquid states,¹⁷ the field has expanded considerably,¹⁸⁻²⁵ and it has been shown to alter reaction kinetics,²⁶⁻²⁹ control reaction selectivity,³⁰ allow for intermolecular energy transfer,³¹ and modification of enzyme activity.³² Recent progresses in chemical reactions making use of polaritons were summarized by Hirai et al.³³ In order to significantly impact chemical reactivity, theoretical investigations has demonstrated that a high coupling strength is required^{34,35} and a recent experimental study has shown a non-linear relationship between the coupling strength and thermodynamics of a chemical reaction.²⁹

Strong light-matter coupling is achieved by interfacing molecules with confined electromagnetic field of resonant cavities tuned to a molecular transition. When a molecular vibrational transition is in the strong coupling regime, two new hybrid states, known as polaritons, are formed,³⁶ separated in energy by the so-called Rabi splitting $\hbar\Omega_R$. Traditionally, polaritons have been engineered with the use of planar cavities, such as Fabry-Pérot resonators confining the electromagnetic fields between two mirrors.¹⁴ Reaching large coupling strengths usually requires saturating the cavity volume with the molecular material, and additionally aligning the transition

dipole moments with the cavity vacuum field.³⁷⁻³⁹

Plasmonics offers an alternative route to strong coupling by confining light down to subwavelength scales with the use of metallic nanoparticles and nanocavities.⁴⁰⁻⁴² Only a tight region of space around the metallic cavity needs to be filled with molecules in order to form polaritons.⁴³ Plasmon resonances of nanoparticles are tunable from the UV to the IR range, and can be used for molecular sensing in the IR range due to nanoscale mode volumes.⁴⁴⁻⁴⁷ However, to improve the sensitivity, new approaches for narrowing the plasmon linewidth are desirable.

The magnitude of the Rabi splitting for a given molecular transition is proportional to the square root of the molecular concentration and the filling factor. Furthermore, the maximal achievable magnitude of the Rabi splitting in the case of saturated mode volume is ultimately bounded by the bulk Rabi splitting $\hbar\Omega_R \sim \sqrt{f}$ (with f being the transition oscillator strength⁴⁸), which is independent on the cavity type.⁴⁹⁻⁵¹ Therefore, new approaches are required to increase the Rabi splitting in order to maximize the effect of the confined electromagnetic field onto molecules, as shown by theoretical studies.^{34,52,53}

In this Letter, we utilize a hierarchical coupling between a Fabry-Pérot cavity, a vibrational absorption band of an organic molecule, and a localized surface plasmon resonance in the mid-IR regime to go beyond the Rabi splitting imposed by the maximal concentration limit⁵⁴. First we show that the coupling of the plasmon and the FP cavity results in an order of magnitude decrease in plasmon's linewidth, an observation rationalized by reduced radiative losses from the plasmon in the cavity⁵⁵. Then, by using numerical and analytical modelling in conjunction to our experimental data, we show a five to nine-fold increase in the total coupling strength, indicating that the plasmon act as an artificial molecule that increases the molecular coupling strength.

Results & discussions

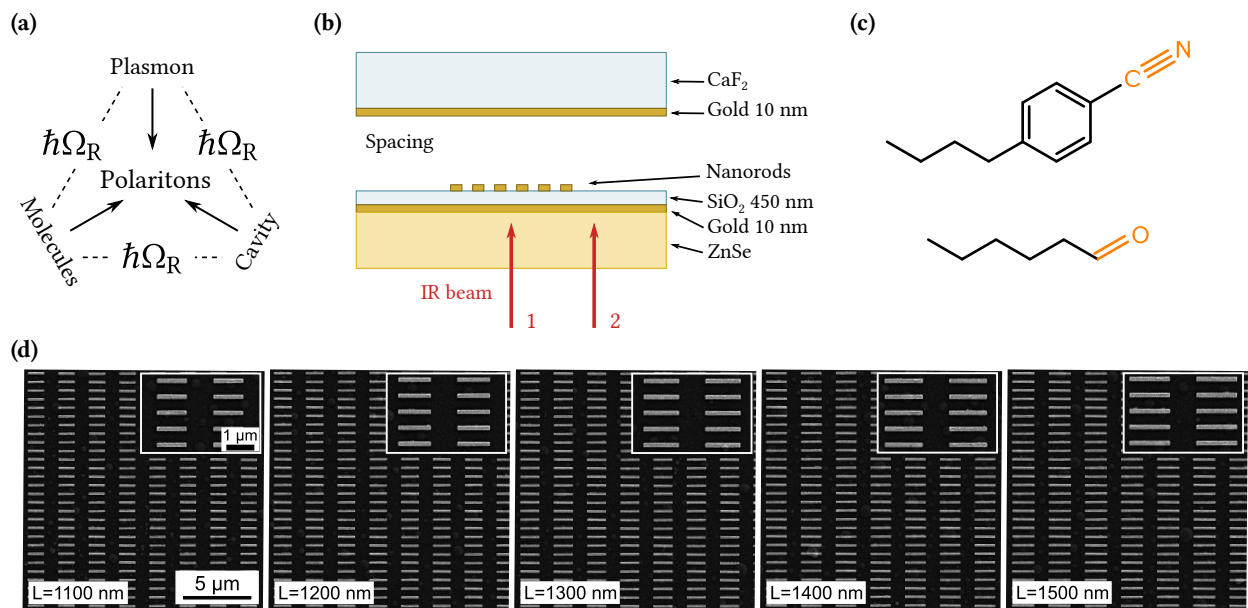


Figure 1 (a) Conceptual diagram of the system in this study. (b) Schematic view of the Fabry-Pérot cavity. Fourier transform infrared spectroscopy microscopy was used to either probe the small area where gold nanorods were deposited (beam 1) or where no rods were present (beam 2). (c) Molecular structure of 4-butylbenzonitrile (top) and hexanal (bottom). Highlighted in orange are the functional groups responsible for the vibrational band coupled to the FP cavity. (d) SEM picture of the gold nanorods.

In this study, we report a method to increase the coupling strength above the limit of \sqrt{C} using a hybrid system composed of a Fabry-Pérot (FP) cavity, an organic molecule, and a localized surface plasmon, in a fashion similar to the one introduced by Bisht et al.⁵⁴ using two-dimensional transition metal dichalcogenides in the visible regime. All three entities are tuned to the same resonance frequency, thereby coupled amongst themselves, creating hybrid polaritons (Figure 1a). The Fabry-Pérot cavities used in the following experiments are composed of IR-transparent substrates (CaF₂ and ZnSe) coated with 10 nm of gold (Figure 1b). The physical distance between the gold mirrors, ranging from 11 to 16 μm , was controlled using a polymer spacer. The cavities were designed with two inlets allowing to inject liquids. The quality factor of an empty cavity was 28, and the free spectral range 496 cm^{-1} (Figure 2a). We choose hexanal and 4-butylbenzonitrile as the organic molecules for this study (Figure 1c). Both are liquids at room temperature and

were processed in neat form. The molecular vibrations of interest are the C=O stretching mode of hexanal and the C≡N stretching mode of 4-butylbenzotrile. These are strong absorption bands centered around 1724 cm^{-1} and 2225 cm^{-1} , with full width at half maxima (FWHM) of 27 and 10 cm^{-1} , respectively (Figure 2b and 2c). The surface plasmon was provided by gold nanorod arrays (size ca. $100\text{ }\mu\text{m}^2$), which were deposited on top a spacer composed of 450 nm of SiO₂ to minimize interference from the gold mirror (Figure 1b). Five different arrays were made, all having equal thickness and spacing but lengths ranging from 1100 to 1500 nm, which gave plasmon resonances covering the energy of both two molecular vibrations and the Fabry-Pérot mode (Figure 2d). The plasmon resonances were broad (FWHM = $621\text{--}1120\text{ cm}^{-1}$) due to radiative losses. This is an intrinsic feature of plasmon arrays in the mid-IR, hampering its use.

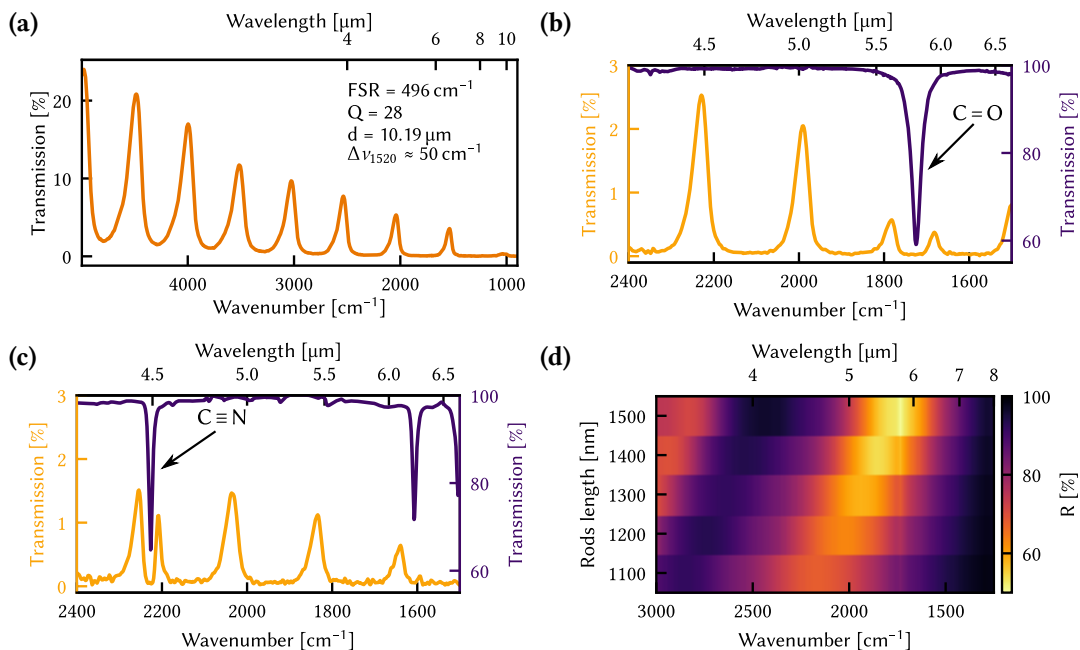


Figure 2 (a) Transmission spectrum of an empty Fabry-Pérot cavity. (b) ATR spectrum of hexanal (purple) showing the C=O absorption band around 1724 cm^{-1} , and transmission spectrum of the FP cavity filled with hexanal (orange). The value of $\hbar\Omega_R$ is 101 cm^{-1} . (c) ATR spectrum of 4-butylbenzotrile (purple) showing the C≡N absorption band around 2225 cm^{-1} , and transmission spectrum of the FP cavity filled with 4-butylbenzotrile (orange). The value of $\hbar\Omega_R$ is 46 cm^{-1} . (d) Reflection map of the five different gold nanorod arrays.

We will first describe the coupling between the cavity and the two molecules, then the cavity and plasmon, and lastly, the complete coupled system with the FP cavity, the plasmon and the

two molecules. Figure 2b and c show a clear normal mode splitting of the vibrational absorption band of the two molecules when placed inside the FP cavity at resonant conditions. This indicates strong coupling between the cavity mode and the carbonyl group of hexanal (Figure 2b), and the cavity mode and the nitrile group of 4-butylbenzotrile (Figure 2c). The resulting formation of vibro-polaritons gives a measured Rabi splitting of 101 cm^{-1} and 46 cm^{-1} for the C=O mode and the C \equiv N mode with the cavity, respectively. The Rabi splittings are larger than both the FWHM of the bare molecular vibrations and the cavity mode, which constitutes further evidence that our system is indeed in the strong-coupling regime. Furthermore the ratio between the coupling strength and the bare transition energy of the vibrations are 2.93% for the C=O band and 1.03% for the C \equiv N band.

Let us now consider the plasmonic arrays inside the FP cavity. With increasing rod length, the plasmon resonance shifts to lower energies (Figure 2d), and the rod length can therefore be viewed as a method of tuning the resonant condition. Moreover, due to intrinsic anisotropy of the rods, the microcavity-plasmon polaritons are formed only along the long axis of the rods, while along the short axis, the bare cavity is recovered. This polariton anisotropy can be probed using polarization-resolved transmission spectroscopy. As shown in Figure 3a, we observe a normal mode splitting of the bare plasmon absorption when the plasmonic arrays are placed inside the FP cavity and the polarizer axis was aligned along the rods. Here, the modes dispersing linearly with the rods length are the polaritonic modes, whereas the vertical modes are uncoupled FP modes, which arise due to polarizer artefacts, as we explain below. Furthermore, we observe an order of magnitude decrease in the linewidth of the resulting polariton compared to the bare plasmon. Similar narrowing was observed in our previous experiments with plasmonic arrays ultra-strongly coupled with FP cavities in the visible to mid-IR range.⁵⁵ The linewidth of closely packed metallic nanorods in the IR region is dominated by radiative losses; but when placed inside a closed cavity, the radiation from the nanorods does not instantaneously leave the cavity, instead bouncing between the mirrors and thus reducing the total resonance linewidth. Consequently, the FWHM of the plasmon polaritons drops to ca. 70 cm^{-1} for all the rods' lengths, as a result

of significantly suppressed radiative damping. Observing that the FWHM of the FP modes are $84 \pm 7.3 \text{ cm}^{-1}$, the linewidth of the cavity is the main limitation of the linewidth of the plasmon polariton (Table S2).

By adding molecules into the cavity, a third coupling component is introduced to the hybrid system. The hexanal C=O band is on resonance with the longest nanorods (Figure 3b), whereas the 4-butylbenzonitrile C \equiv N band is on resonance with the shortest nanorods (Figure 3c). This time more FP modes are present in the same spectral range due to the larger background refractive index of the molecules compared to air. Furthermore, the polaritonic modes linewidths are again reduced by the cavity mirrors, showing that the FP cavity mode limits the polariton linewidth independent of the medium inside the cavity.

In order to gain further understanding of the experimental results, we performed numerical modelling of the coupled systems using FDTD (Figure 3d-f, Figure S1-3). Simulated normal-incidence transmission spectra demonstrate a good agreement with the experimental spectra for both plasmonic structures, and composite plasmon-molecule ones. Specifically, the observed polaritonic modes linearly disperse with the rods length, however, the dispersion is less pronounced than for uncoupled rods (gray dots). This is a consequence of intermixing between highly dispersive plasmonic modes and non-dispersive FP modes (all arrays were placed in the same FP cavity). The results also suggest that uncoupled FP transmission peaks found in the measured spectra are an artifact resulting from non-ideal polarization alignment. To confirm that, we simulated transmission spectra of the coupled systems illuminated with plane wave polarized linearly at an angle of 20 degrees with respect to the nanorod longer axis. The resulting spectra clearly exhibit uncoupled FP resonances (Figure S2).

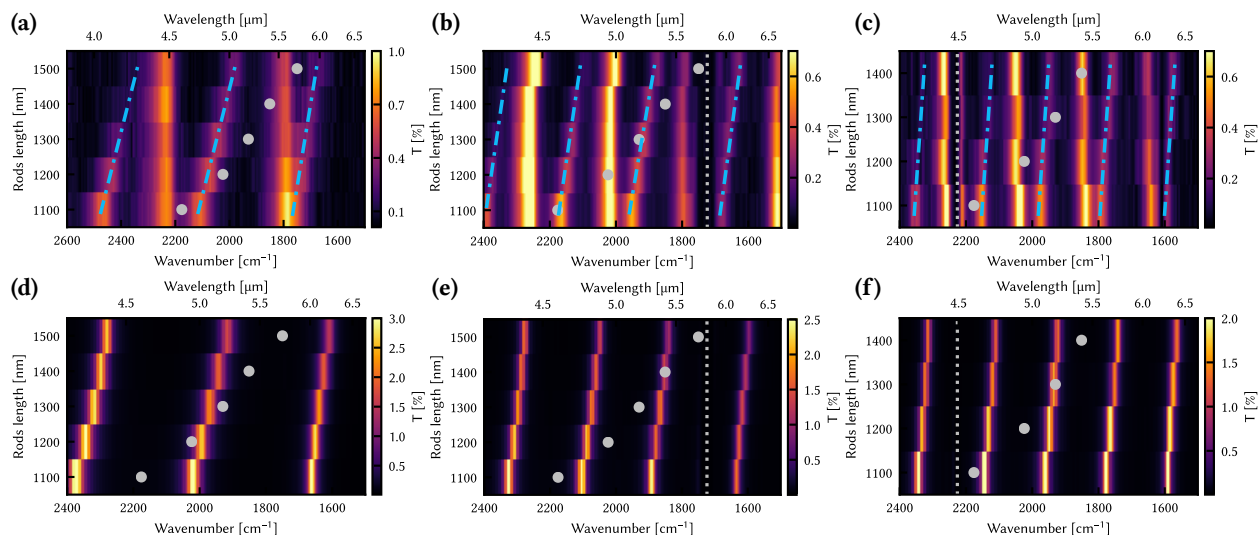


Figure 3 (a)-(c) Transmission maps of the gold rods inside the Fabry-Pérot cavity, containing air, hexanal, or 4-butylbenzotrinitrile, respectively. All three were measured with a polarizer along the long axis of the rods. The blue dash-dot lines highlight the newly formed polaritonic states, the residual vertical modes are artifact due to non-ideal polarization alignment. (d)-(f) Simulated spectra of the same systems. The gray dashed line indicates the absorption band of interest of the molecules, and the gray dots indicate the plasmon absorption maximum.

Next, to ensure that the observed dispersions are a result of the interaction between the three components in the hybrid system, transmission spectra of the system with a polarizer perpendicular to the nanorods' long axis were measured. The results are shown in Figure S6 (numerical modeling in Figure S1). As expected, when the contribution of the plasmonic array is removed by the polarizer, the transmission spectra are the same as when probing the system beside the array (Figure 2b and c). Likewise, the values of $\hbar\Omega_R$ with a perpendicular polarizer are 46 cm^{-1} and 101 cm^{-1} for the $\text{C}\equiv\text{N}$ and $\text{C}=\text{O}$ vibrations, respectively, which are the same values as we observed when when probing next to the plasmonic array.

Theoretical analysis

In order to extract coupling strengths and confirm that the plasmonic array acts as an artificial molecule to enhance the total coupling strength of the system, we turn to theoretical analysis of the experimental results. This analysis is essentially based on the coupled harmonic oscillator

algebra in the simplest possible implementation. Furthermore, this analysis requires several rather crude assumptions, which may be false in general, but are satisfactory for the goal of extracting the collective coupling constants.

In view of the above remark, we describe the cavity by a set of M orthogonal Fabry-Pérot eigenmodes with equidistant frequencies $\omega_m = m\omega_1$, each coupling to the molecular resonance with a certain coupling constant. For pure molecular samples, all the N molecules residing within the cavity can be roughly approximated by a single collective harmonic oscillator with the resonant frequency of a single molecule ω_0 , and the collective dipole moment $\mu\sqrt{N}$ (this approximation is rather crude, but for the purposes of extracting collective molecular, plasmonic, and intermixed situations, is sufficiently adequate). As we are far from the ultrastrong coupling regime in this case, we employ the multimode coupled-harmonic oscillator Hamiltonian, including M lowest Fabry-Pérot modes, and the single harmonic oscillator describing the collective molecular resonance:

$$\hat{H}_{mol} = \sum_{m=1}^M \hbar\omega_m \hat{a}_m^\dagger \hat{a}_m + \hbar\omega_0 \hat{b}^\dagger \hat{b} + \sum_{m=1}^M \hbar g_m (\hat{a}_m^\dagger \hat{b} + \hat{a}_m \hat{b}^\dagger) \quad (1)$$

where \hat{a} and \hat{b} are the annihilation operators of the m -th cavity mode and that of the molecular resonance, respectively, and g_m is the coupling constant.

The coupling constant to the m -th cavity mode is given by the standard expression following from the expansion of the minimal coupling Hamiltonian in the Coulomb gauge:^{55,56} $g_m = \mu\sqrt{\rho}\mathcal{E}_{vac}\omega_0/\omega_m$, where μ is the dipole moment of transitions with density ρ , and \mathcal{E}_{vac} is the cavity vacuum field. Each molecule in the cavity, in principle, will experience a different vacuum field depending on its position. But to simplify the analysis, we will assume that all molecules experience the same average vacuum field $\mathcal{E}_{vac} \sim \sqrt{\hbar\omega_m/L_{cav}}$. Thus, the coupling strength with the m -th cavity mode takes the form $g_m = g_0\sqrt{\hbar\omega_m\omega_0/\omega_m}$, where g_0 is a scaling constant that includes the molecular dipole moment, the molecular concentration, and the cavity mode volume.

The coupled Fabry-Pérot system exhibits transmission peaks at its polaritonic resonances, corresponding to the eigenvalues of the Hamiltonian (Eq. 1). Therefore, we estimate the cavity-molecule coupling strength by fitting the energies of the transmission peaks by the eigenvalues

of Hamiltonian Eq. 1 accounting for the $M = 20$ lowest cavity modes. Simply estimating the number of supported FP modes as $M \sim \omega_{plasma}/\omega_1$ with ω_{plasma} being the plasma frequency of the mirror's metal, we find that these cavities support over 100 eigenmodes; however, the energy spectrum of Eq. (1) quickly converges and the presence of high energy modes only weakly affects the eigenvalues in the relevant spectral range. The cavity thickness L_{cav} for each sample was first roughly estimated by counting the number of transmission peaks q away from the molecular resonance in a certain wavelength range $\lambda_1 \dots \lambda_2$; next, it was varied during the fitting to yield better agreement between measured and theoretical dispersions (see Methods). Since in the multi-mode system, the coupling strength is dependent on the FP mode order and the frequency, to make a reasonable comparison we estimate the coupling strength at zero detuning. That is, with the particular FP mode, (near-)resonant with the molecular transition. By fitting the eigenvalues to the positions of measured transmission peaks (see Figure S5), we obtain the hexanal-cavity system zero-detuning coupling strength (with the 7-th FP mode of a 14.25 μm thick cavity) of about 41 cm^{-1} . Remarkably, this value is close to the bulk polariton coupling strength of hexanal $g_{bulk} = \omega_p \sqrt{f/\epsilon_\infty}/2 \approx 49 \text{ cm}^{-1}$, which describes the photon-molecule interaction strength in an unbounded homogeneous molecular medium.⁵⁷ Similarly, for the 4-butylbenzonitrile-cavity system, we obtain the zero-detuning coupling strength (with the 11-th mode of a 16.15 μm thick cavity) of about 18 cm^{-1} , which is also comparable to the respective bulk coupling strength of 4-butylbenzonitrile (21 cm^{-1}).

In a similar way, we analyze the cavity-nanorod system, except that a single mode collective molecular resonance is now replaced by a single mode plasmonic resonance. The nanorod array can be described by a single harmonic oscillator with energy ω_{pl} which disperses with the nanorod length L_{rod} (Figure S3a). Since it is positioned in a specific horizontal plane inside the cavity at a height z above the bottom mirror, the coupling strength takes the form $g_m = g_0 \sqrt{\hbar \omega_m} \sin \frac{zm\pi}{L_{cav}} \omega_0/\omega_m$, which takes into account the transverse distribution of the vacuum cavity field. Strictly speaking, the coupling strength will also disperse with the nanorods length. Longer nanorods will have a larger transition dipole moment, but the increasing length at the same time reduces their surface

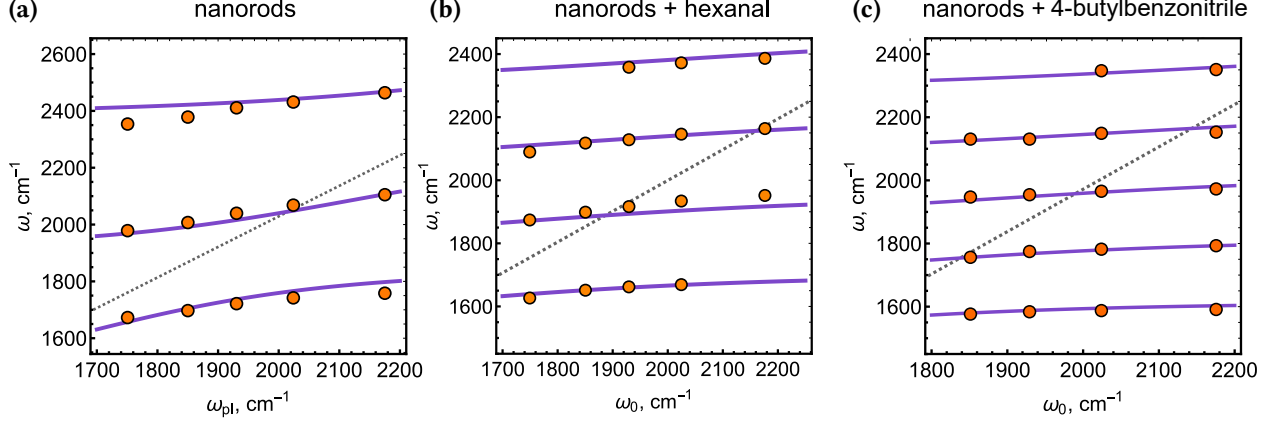


Figure 4 Hamiltonian analysis of the experimental data. **(a)** Fitting of the measured transmission peaks of the coupled nanorod-cavity system (circles) with eigenvalues of the multimode JC Hamiltonian (lines). **(b)** The same as (a) for the hybrid hexanal-nanorod system. **(c)** The same as (a) for the hybrid 4-butylbenzotrile-nanorod system.

density. The exact scaling law of the nanorod dipole moment with length is not known, but we will assume for simplicity that the product $\mu \sqrt{\rho}$ is constant in the studied range of L_{rod} between 1100 and 1500 nm (for comparison, we observed less than 50% variation of this product upon an octave variation of nanorods length in a similar system⁵⁵). Hence, we replace ω_0 in the Hamiltonian (Eq. 1) with ω_{pl} and substitute the corresponding coupling strength; note that $n_b = 1$ (the background refractive index of the cavity medium) for plasmonic samples. By fitting the measured dispersion of transmission peaks with the Hamiltonian eigenvalues, Figure 4a, we obtain the resonant coupling strength (with the 4-th FP mode of a 10.5 μm thick cavity) of about 163 cm^{-1} .

Next we switch to the complete cavity-plasmon-molecule systems. The key idea of our experiment is to show that plasmonic nanorods can act as artificial molecules with the oscillator strength significantly exceeding molecular ones, joining the real molecules in a single collective oscillator, and thus boosting the coupling strength and Rabi splitting. Therefore, we model the plasmon-molecule hybrid as a single collective oscillator characterized by the plasmon energy ω_0 that couples to Fabry-Pérot cavity modes with coupling strength g_m . The coupling strength of this hybrid oscillator to the m -th cavity mode takes the form $g_m = g_0 \sqrt{\hbar \omega_m} \sin \frac{zm\pi}{L_{cav}} \omega_0 / \omega_m$, where z is the position of the nanorod array above the bottom mirror (exactly like in the cavity-nanorod system). This approach is justified by the fact that the plasmon provide most of the coupling strength.

By fitting the measured dispersion of transmission peaks of the hybrid plasmon-hexanal-cavity system with the Hamiltonian eigenvalues, Figure 4b, we obtain a resonant coupling strength (with the 8-th FP mode of a 12.9 μm thick cavity and $z = 500$ nm) of about 198 cm^{-1} . Despite the number of assumptions made in the analysis, the Hamiltonian fit shows a good agreement with measured transmission peaks. Similarly, for the hybrid plasmon-4-butylbenzotrile-cavity system we obtain a resonant coupling strength of 181 cm^{-1} (with the 11-th FP mode of a 15.9 μm thick cavity), Figure 4c.

The simple analysis performed above suggests that the molecules and the nanorods act indeed as a collective oscillator with the effective coupling strength approximately given by the sum of the two individual coupling strengths, $g_{eff} \sim g_{pl} + g_{mol}$. Thus, the presence of the plasmon boosts the effective coupling strength of 4-butylbenzotrile and hexanal with the cavity mode by 9 times and 5 times, respectively. The results of our experiment and its subsequent analysis suggest that using the plasmon resonance with large oscillator strength indeed allows to boost the effective coupling strength beyond the bulk limit bounded by the molecular concentration. Of course, this addition of the plasmonic meta-atoms does not modify the molecular oscillator strength per se, but rather modifies the effective polaritonic spectrum of the hybrid system in the vibrational strong coupling regime. This in turn may potentially affect chemical reactions whose rate was claimed to depend on the vacuum Rabi splitting in the recent literature³⁰.

Conclusion

In summary, our hybrid Fabry-Pérot cavities show that the addition of a plasmonic array to the standard molecular vibro-polaritonic system increases the total coupling strength by almost an order of magnitude for a nitrile absorption band and five times for a carbonyl absorption band. Increasing the coupling strength beyond the molecular concentration limit, dismantle the crucial obstacle for reaching the ultra-strong coupling regime using organic molecules. Furthermore, precisely controlling the coupling strength, not only with the molecular concentration, but also

with the density of the plasmonic array, allows molecules at small concentrations to reach the strong coupling limit. One can in a sense view the plasmonic array as a form of "catalyst", that enables any on-resonance molecular transition, regardless of molecular concentration and transition dipole moment strength, to reach the strong coupling regime. Furthermore, the cavity reduces the radiative damping from the plasmon, sharpening the polariton linewidth with more than an order of magnitude. Together with the spectral tuning ability, such sharp linewidths may allow for mode-selective chemical sensing in the mid-IR. The approach described here is not limited to infrared transitions, but can also be transposed to electronic transitions. For these reasons, we suggest that our hybrid system will be an ideal platform to explore the promising potential of polaritonic chemistry, the ultra-strong coupling regime, as well as provide an approach to mode-selective mid-IR sensing.

Acknowledgement

B.M., D.G.B. and T.O.S. acknowledge financial support from the Swedish Research Council (under VR Miljö project, grant No: 2016-06059) and the Knut and Alice Wallenberg Foundation. K.B. and M.H. acknowledge financial support from the European Research council (ERC-2017-StG-757733) and the Knut and Alice Wallenberg Foundation (KAW 2017.0192).

Supporting Information Available

The supporting information contains the following sections.

- S1: Methods
- S2: Additional figures

References

1. Ebbesen, T. W. Hybrid Light–Matter States in a Molecular and Material Science Perspective. *Acc. Chem. Res.* **2016**, *49*, 2403–2412.
2. Ribeiro, R. F.; Martínez-Martínez, L. A.; Du, M.; Campos-Gonzalez-Angulo, J.; Yuen-Zhou, J. Polariton chemistry: controlling molecular dynamics with optical cavities. *Chem. Sci.* **2018**, *9*, 6325–6339.
3. Flick, J.; Rivera, N.; Narang, P. Strong light-matter coupling in quantum chemistry and quantum photonics. *Nanophotonics* **2018**, *7*, 1479–1501.
4. Hertzog, M.; Wang, M.; Mony, J.; Börjesson, K. Strong light–matter interactions: a new direction within chemistry. *Chem. Soc. Rev.* **2019**, *48*, 937–961.
5. Schwartz, T.; Hutchison, J. A.; Genet, C.; Ebbesen, T. W. Reversible Switching of Ultrastrong Light-Molecule Coupling. *Phys. Rev. Lett.* **2011**, *106*, 196405.
6. Hutchison, J. A.; Schwartz, T.; Genet, C.; Devaux, E.; Ebbesen, T. W. Modifying Chemical Landscapes by Coupling to Vacuum Fields. *Angew. Chem. Int. Ed.* **2012**, *51*, 1592–1596.
7. Orgiu, E.; George, J.; Hutchison, J. A.; Devaux, E.; Dayen, J. F.; Doudin, B.; Stellacci, F.; Genet, C.; Schachenmayer, J.; Genes, C.; Pupillo, G.; Samorì, P.; Ebbesen, T. W. Conductivity in organic semiconductors hybridized with the vacuum field. *Nat. Mater.* **2015**, *14*, 1123–1129.
8. Coles, D. M.; Somaschi, N.; Michetti, P.; Clark, C.; Lagoudakis, P. G.; Savvidis, P. G.; Lidzey, D. G. Polariton-mediated energy transfer between organic dyes in a strongly coupled optical micro-cavity. *Nat. Mater.* **2014**, *13*, 712–719.
9. Zhong, X.; Chervy, T.; Wang, S.; George, J.; Thomas, A.; Hutchison, J. A.; Devaux, E.; Genet, C.; Ebbesen, T. W. Non-Radiative Energy Transfer Mediated by Hybrid Light-Matter States. *Angew. Chem. Int. Ed.* **2016**, *128*, 6310–6314.

10. Zhong, X.; Chervy, T.; Zhang, L.; Thomas, A.; George, J.; Genet, C.; Hutchison, J. A.; Ebbesen, T. W. Energy Transfer between Spatially Separated Entangled Molecules. *Angew. Chem. Int. Ed.* **2017**, *56*, 9034–9038.
11. Stranius, K.; Hertzog, M.; Börjesson, K. Selective manipulation of electronically excited states through strong light–matter interactions. *Nat. Commun.* **2018**, *9*, 2273.
12. Munkhbat, B.; Wersäll, M.; Baranov, D. G.; Antosiewicz, T. J.; Shegai, T. Suppression of photo-oxidation of organic chromophores by strong coupling to plasmonic nanoantennas. *Sci. Adv.* **2018**, *4*, eaas9552.
13. Peters, V. N.; Faruk, M. O.; Asane, J.; Alexander, R.; Peters, D. A.; Prayakarao, S.; Rout, S.; Noginov, M. A. Effect of strong coupling on photodegradation of the semiconducting polymer P3HT. *Optica* **2019**, *6*, 318–325.
14. Shalabney, A.; George, J.; Hutchison, J.; Pupillo, G.; Genet, C.; Ebbesen, T. W. Coherent coupling of molecular resonators with a microcavity mode. *Nat. Commun.* **2015**, *6*, 5981.
15. Long, J. P.; Simpkins, B. S. Coherent Coupling between a Molecular Vibration and Fabry–Perot Optical Cavity to Give Hybridized States in the Strong Coupling Limit. *ACS Photonics* **2015**, *2*, 130–136.
16. Simpkins, B. S.; Fears, K. P.; Dressick, W. J.; Spann, B. T.; Dunkelberger, A. D.; Owrutsky, J. C. Spanning Strong to Weak Normal Mode Coupling between Vibrational and Fabry–Pérot Cavity Modes through Tuning of Vibrational Absorption Strength. *ACS Photonics* **2015**, *2*, 1460–1467.
17. George, J.; Shalabney, A.; Hutchison, J. A.; Genet, C.; Ebbesen, T. W. Liquid-Phase Vibrational Strong Coupling. *J. Phys. Chem. Lett.* **2015**, *6*, 1027–1031.
18. Hertzog, M.; Börjesson, K. The Effect of Coupling Mode in the Vibrational Strong Coupling Regime. *ChemPhotoChem* **2020**, *4*, 612–617.

19. Menghrajani, K. S.; Fernandez, H. A.; Nash, G. R.; Barnes, W. L. Hybridization of Multiple Vibrational Modes via Strong Coupling Using Confined Light Fields. *Adv. Opt. Mater.* **2019**, *7*, 1900403.
20. Dunkelberger, A. D.; Grafton, A. B.; Vurgaftman, I.; Öney O. Soykal,; Reinecke, T. L.; Davidson, R. B.; Simpkins, B. S.; Owrutsky, J. C. Saturable Absorption in Solution-Phase and Cavity-Coupled Tungsten Hexacarbonyl. *ACS Photonics* **2019**, *6*, 2719–2725.
21. Pietron, J. J.; Fears, K. P.; Owrutsky, J. C.; Simpkins, B. S. Electrochemical Modulation of Strong Vibration–Cavity Coupling. *ACS Photonics* **2019**, *7*, 165–173.
22. Xiang, B.; Ribeiro, R. F.; Li, Y.; Dunkelberger, A. D.; Simpkins, B. B.; Yuen-Zhou, J.; Xiong, W. Manipulating optical nonlinearities of molecular polaritons by delocalization. *Sci. Adv.* **2019**, *5*, eaax5196.
23. Menghrajani, K. S.; Nash, G. R.; Barnes, W. L. Vibrational Strong Coupling with Surface Plasmons and the Presence of Surface Plasmon Stop Bands. *ACS Photonics* **2019**, *6*, 2110–2116.
24. Menghrajani, K. S.; Barnes, W. L. Strong coupling beyond the light-line. *ACS Photonics* **2020**, *7*, 2448–2459.
25. Takele, W. M.; Wackenhut, F.; Piatkowski, L.; Meixner, A. J.; Waluk, J. Multimode Vibrational Strong Coupling of Methyl Salicylate to a Fabry–Pérot Microcavity. *J. Phys. Chem. B* **2020**, *124*, 5709–5716.
26. Lather, J.; Bhatt, P.; Thomas, A.; Ebbesen, T. W.; George, J. Cavity Catalysis by Cooperative Vibrational Strong Coupling of Reactant and Solvent Molecules. *Angew. Chem. Int. Ed.* **2019**, *58*, 10635–10638.
27. Hirai, K.; Takeda, R.; Hutchison, J. A.; Uji-i, H. Modulation of Prins Cyclization by Vibrational Strong Coupling. *Angew. Chem. Int. Ed.* **2020**, *132*, 5370–5373.

28. Pang, Y.; Thomas, A.; Nagarajan, K.; Vergauwe, R. M. A.; Joseph, K.; Patrahau, B.; Wang, K.; Genet, C.; Ebbesen, T. W. On the Role of Symmetry in Vibrational Strong Coupling: The Case of Charge-Transfer Complexation. *Angew. Chem. Int. Ed.* **2020**, *132*, 10522–10526.
29. Thomas, A.; Jayachandran, A.; Lethuillier-Karl, L.; Vergauwe, R. M.; Nagarajan, K.; Devaux, E.; Genet, C.; Moran, J.; Ebbesen, T. W. Ground state chemistry under vibrational strong coupling: dependence of thermodynamic parameters on the Rabi splitting energy. *Nanophotonics* **2020**, *9*, 249–255.
30. Thomas, A.; Lethuillier-Karl, L.; Nagarajan, K.; Vergauwe, R. M. A.; George, J.; Chervy, T.; Shalabney, A.; Devaux, E.; Genet, C.; Moran, J.; Ebbesen, T. W. Tilting a ground-state reactivity landscape by vibrational strong coupling. *Science* **2019**, *363*, 615–619.
31. Xiang, B.; Ribeiro, R. F.; Du, M.; Chen, L.; Yang, Z.; Wang, J.; Yuen-Zhou, J.; Xiong, W. Intermolecular vibrational energy transfer enabled by microcavity strong light–matter coupling. *Science* **2020**, *368*, 665–667.
32. Vergauwe, R. M. A.; Thomas, A.; Nagarajan, K.; Shalabney, A.; George, J.; Chervy, T.; Seidel, M.; Devaux, E.; Torbeev, V.; Ebbesen, T. W. Modification of Enzyme Activity by Vibrational Strong Coupling of Water. *Angew. Chem. Int. Ed.* **2019**, *58*, 15324–15328.
33. Hirai, K.; Hutchison, J. A.; Uji-i, H. Recent Progress of Vibropolaritonic Chemistry. *ChemPlusChem* **2020**, *85*, 1981.
34. Galego, J.; Climent, C.; Garcia-Vidal, F. J.; Feist, J. Cavity Casimir-Polder Forces and Their Effects in Ground-State Chemical Reactivity. *Phys. Rev. X* **2019**, *9*.
35. Hiura, H.; Shalabney, A. A Reaction Kinetic Model for Vacuum-Field Catalysis Based on Vibrational Light-Matter Coupling. *ChemRxiv* **2019**, chemrxiv.9275777.v1.
36. Khitrova, G.; Gibbs, H. M.; Kira, M.; Koch, S. W.; Scherer, A. Vacuum Rabi splitting in semiconductors. *Nat. Phys.* **2006**, *2*, 81–90.

37. Hertzog, M.; Rudquist, P.; Hutchison, J. A.; George, J.; Ebbesen, T. W.; Börjesson, K. Voltage-controlled switching of strong light–matter interactions using liquid crystals. *Chem. Eur. J.* **2017**, *23*, 18166–18170.
38. Berghuis, A. M.; Serpenti, V.; Ramezani, M.; Wang, S.; Rivas, J. G. Light–Matter Coupling Strength Controlled by the Orientation of Organic Crystals in Plasmonic Cavities. *J. Phys. Chem. C* **2020**, *124*, 12030–12038.
39. Roux, F. L.; Taylor, R. A.; Bradley, D. D. C. Enhanced and Polarization-Dependent Coupling for Photoaligned Liquid Crystalline Conjugated Polymer Microcavities. *ACS Photonics* **2020**, *7*, 746–758.
40. Savasta, S.; Saija, R.; Ridolfo, A.; Stefano, O. D.; Denti, P.; Borghese, F. Nanopolaritons: Vacuum Rabi Splitting with a Single Quantum Dot in the Center of a Dimer Nanoantenna. *ACS Nano* **2010**, *4*, 6369–6376.
41. Manjavacas, A.; de Abajo, F. J. G.; Nordlander, P. Quantum Plexcitonics: Strongly Interacting Plasmons and Excitons. *Nano Lett.* **2011**, *11*, 2318–2323.
42. Schlather, A. E.; Large, N.; Urban, A. S.; Nordlander, P.; Halas, N. J. Near-Field Mediated Plexcitonic Coupling and Giant Rabi Splitting in Individual Metallic Dimers. *Nano Lett.* **2013**, *13*, 3281–3286.
43. Chikkaraddy, R.; de Nijs, B.; Benz, F.; Barrow, S. J.; Scherman, O. A.; Rosta, E.; Demetriadou, A.; Fox, P.; Hess, O.; Baumberg, J. J. Single-molecule strong coupling at room temperature in plasmonic nanocavities. *Nature* **2016**, *535*, 127–130.
44. Rodrigo, D.; Limaj, O.; Janner, D.; Etezadi, D.; de Abajo, F. J. G.; Pruneri, V.; Altug, H. Mid-infrared plasmonic biosensing with graphene. *Science* **2015**, *349*, 165–168.
45. Limaj, O.; Etezadi, D.; Wittenberg, N. J.; Rodrigo, D.; Yoo, D.; Oh, S.-H.; Altug, H. Infrared

- Plasmonic Biosensor for Real-Time and Label-Free Monitoring of Lipid Membranes. *Nano Lett.* **2016**, *16*, 1502–1508.
46. Singh, P. SPR Biosensors: Historical Perspectives and Current Challenges. *Sens. Actuators, B* **2016**, *229*, 110–130.
 47. Leitis, A.; Tittl, A.; Liu, M.; Lee, B. H.; Gu, M. B.; Kivshar, Y. S.; Altug, H. Angle-multiplexed all-dielectric metasurfaces for broadband molecular fingerprint retrieval. *Sci. Adv.* **2019**, *5*, eaaw2871.
 48. Novotny, L.; Hecht, B. *Principles of Nano-Optics*; Cambridge University Press, 2006.
 49. Törmä, P.; Barnes, W. L. Strong coupling between surface plasmon polaritons and emitters: a review. *Rep. Prog. Phys.* **2014**, *78*, 013901.
 50. del Pino, J.; Feist, J.; Garcia-Vidal, F. J. Quantum theory of collective strong coupling of molecular vibrations with a microcavity mode. *New J. Phys.* **2015**, *17*, 053040.
 51. Baranov, D. G.; Wersäll, M.; Cuadra, J.; Antosiewicz, T. J.; Shegai, T. Novel Nanostructures and Materials for Strong Light–Matter Interactions. *ACS Photonics* **2017**, *5*, 24–42.
 52. Climent, C.; Galego, J.; Garcia-Vidal, F. J.; Feist, J. Plasmonic Nanocavities Enable Self-Induced Electrostatic Catalysis. *Angew. Chem. Int. Ed.* **2019**, *58*, 8698–8702.
 53. Triana, J.; Herrera, F. Self-Dissociation of Polar Molecules in a Confined Infrared Vacuum. [10.26434/chemrxiv.12702419.v1](https://doi.org/10.26434/chemrxiv.12702419.v1) **2020**,
 54. Bisht, A.; Cuadra, J.; Wersäll, M.; Canales, A.; Antosiewicz, T. J.; Shegai, T. Collective Strong Light-Matter Coupling in Hierarchical Microcavity-Plasmon-Exciton Systems. *Nano Lett.* **2018**, *19*, 189–196.
 55. Baranov, D. G.; Munkhbat, B.; Zhukova, E.; Bisht, A.; Canales, A.; Rousseaux, B.; Johansson, G.; Antosiewicz, T. J.; Shegai, T. Ultrastrong coupling between nanoparticle plasmons and cavity photons at ambient conditions. *Nat. Commun.* **2020**, *11*, 5561.

56. Liberato, S. D. Light-Matter Decoupling in the Deep Strong Coupling Regime: The Breakdown of the Purcell Effect. *Phys. Rev. Lett.* **2014**, *112*, 016401.
57. Hopfield, J. J. Theory of the Contribution of Excitons to the Complex Dielectric Constant of Crystals. *Phys. Rev.* **1958**, *112*, 1555–1567.

Supporting information for

Enhancing vibrational light-matter coupling strength beyond the molecular concentration limit using plasmonic arrays

Manuel Hertzog,[†] Battulga Munkhbat,[‡] Denis G. Baranov,[‡] Timur O. Shegai,^{*,‡}
and Karl Börjesson^{*,†}

[†]*Department of Chemistry and Molecular Biology, University of Gothenburg, Kemigården 4, 412
96, Gothenburg, Sweden*

[‡]*Department of Physics, Chalmers University of Technology, 412 96, Gothenburg, Sweden*

E-mail: timurs@chalmers.se; karl.borjesson@gu.se

Contents

S1 Methods		2
S1.1 Cavity preparation		2
S1.2 Optical characterization		2
S1.3 Numerical modelling		3
S1.4 Cavity thickness determination		4
S2 Additional figures		5
References		8

S1 Methods

S1.1 Cavity preparation

Fabry-Pérot cavities were produced using a demountable liquid cell for IR spectroscopy (Omni Cell, Specac) with CaF₂ and ZnSe optical windows. The substrates were cleaned with acetone and isopropanol (IPA), and dried under nitrogen. The gold mirrors (10 nm) were deposited using a DC magnetron sputterer (HEX, Korvus Technologies) or electron beam (e-beam) evaporator. Then, a 450 nm SiO₂ layer was deposited by sputtering on top of the freshly prepared bottom gold mirror. Lattice arrays of gold nanorods with various lengths and densities were fabricated using a standard e-beam lithography (EBL) technique. In brief, a 110 nm of poly(methyl methacrylate) PMMA layer was spin coated on top of the SiO₂ layer, and baked at 180 °C for 5 min. Then, samples were exposed using a JEOL JBX 9300FS electron beam lithography system according to pre-designed pattern of nanorods with a fixed width of 150 nm and various lengths, ranging from 1100 nm to 1500 nm with a step of 100 nm. The edge to edge distances were 1000 nm and 150 nm along the longer and shorter axis of the rods, respectively. After the e-beam exposure, the samples were developed under a MIBK:IPA (1:3) solution and rinsed with IPA, and dried under nitrogen gas. Afterwards, 2 nm of chromium and 40 nm of gold were deposited with e-beam evaporation. Lastly, a lift-off process was done in acetone at 60 °C for ca. 30 min, and rinsed with IPA and water, to form the gold nanorods. The physical distance between the mirrors was controlled using a Mylar spacer (Specac) of 6 μm and the fine adjustment of the thickness was done using adjustment screws on the microfluidic cell. Finally, hexanal (Sigma-Aldrich) and 4-butylbenzotrile (Sigma-Aldrich) were injected into the cavity using a syringe connected to the inlet of the cell. All chemicals were used without further purification.

S1.2 Optical characterization

Infrared spectra were recorded using an FT-IR microscope (Hyperion 3000, Bruker), using a Schwarzschild-objective 15x objective (NA=0.4) and a linear polarizer parallel and perpendicular

along the long axis of the nanorods, connected to an FT-IR spectrometer (Vertex 70v, Bruker) in reflection or transmission mode. All measurements were recorded with a liquid nitrogen cooled MCT detector at a resolution of 4 cm^{-1} using 512 scans. Furthermore, ATR spectra were recorded using an FT-IR spectrometer (Invenio-R, Bruker) coupled to a PLATINUM ATR accessory (Bruker). The ATR spectra were recorded using a DLaTGS detector with a resolution of 4 cm^{-1} and 64 scans. Morphology of the samples was characterized using a Zeiss (Germany) scanning electron microscope (SEM ULTRA 55 FEG).

S1.3 Numerical modelling

FDTD simulations of the electromagnetic response of the coupled plasmon-cavity and plasmon-molecule-cavity systems were performed using a commercial software (FDTD Solutions, Lumerical, Inc., Canada). Transmission and absorption spectra, as well as electromagnetic field distributions, were obtained with the use of a linearly polarized normally incident plane wave source and periodic boundary conditions. The plane wave was polarized either along the nanorods or perpendicular to them. The permittivity of gold was approximated by interpolating the experimental data from Johnson and Christie¹ in the range $3\text{ }\mu\text{m}$ to $8\text{ }\mu\text{m}$. The mesh parameter was set to 4 in all simulations.

In order to obtain the optical response of hexanal and 4-butylbenzonitrile in the infrared region a multi-Lorentz oscillator model was used:²

$$\tilde{n}(k) = \sqrt{n_b^2 - \sum_{j=0}^N \frac{f_j}{k^2 - k_{0j}^2 + ik\gamma_j}} \quad (\text{S1})$$

where, n_b is the background refractive index, f_j is the oscillator strength, k_{0j} is the resonant wave vector and γ_j is the damping constant, i.e. the full width at half maximum of the j^{th} oscillator.

S1.4 Cavity thickness determination

The cavity thickness d was measured using the following equation:

$$d = \frac{q}{2n} \left(\frac{\lambda_i \lambda_j}{\lambda_i - \lambda_j} \right) \quad (\text{S2})$$

where, $\lambda_{i,j}$ are the wavelengths of the Fabry-Pérot mode, n the refractive index and q is an integer number given by $q = j - i$.

Table 1. Measured thicknesses of the FP cavities.

Cavity	FP/rods	FP/hex	FP/4-butyl	FP/rods/hex	FP/rods/4-butyl
d [μm]	11.6	14.9	16.3	13.4	16.2

S2 Additional figures

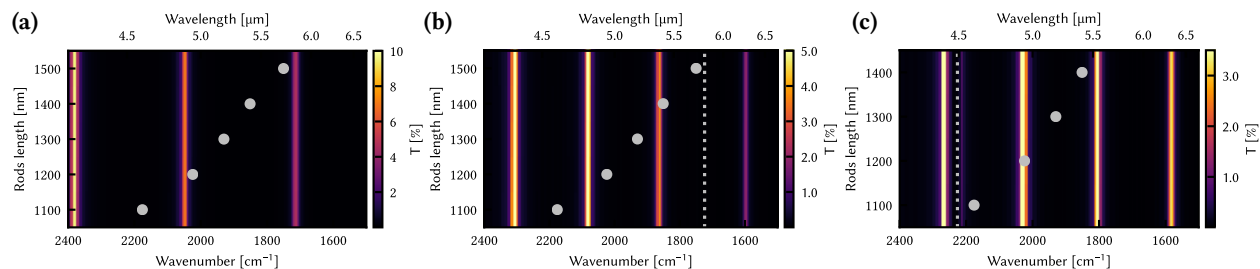


Figure S1. (a)-(c) Simulated transmission spectra of the gold rods inside the Fabry-Pérot cavity, without molecules, with hexanal, and with 4-butylbenzotrile, respectively. All three are simulated with a polarizer perpendicular to the long axis of the rods. The gray dashed line indicates the absorption band of interest of the molecules and the gray dots indicates the absorption maximum of the bare plasmons.

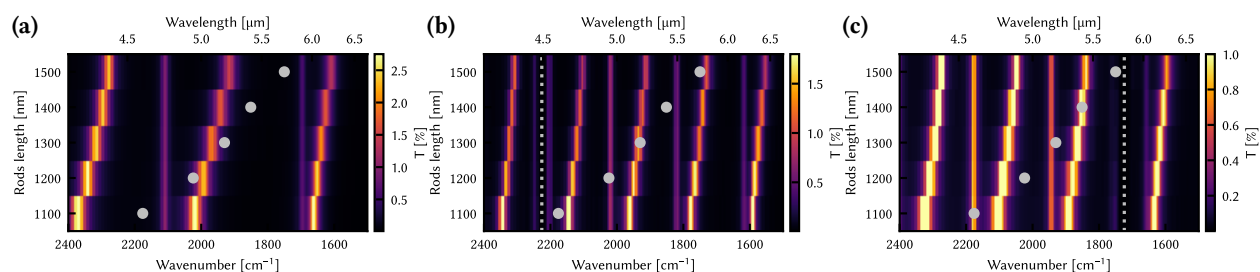


Figure S2. (a)-(c) Simulated transmission spectra of the gold rods inside the Fabry-Pérot cavity, without molecules, with hexanal, and with 4-butylbenzotrile, respectively. All three are simulated with a polarizer at 20° relatively to the long axis of the rods. The gray dashed line indicates the absorption band of interest of the molecules and the gray dots indicates the absorption maximum of the bare plasmons.

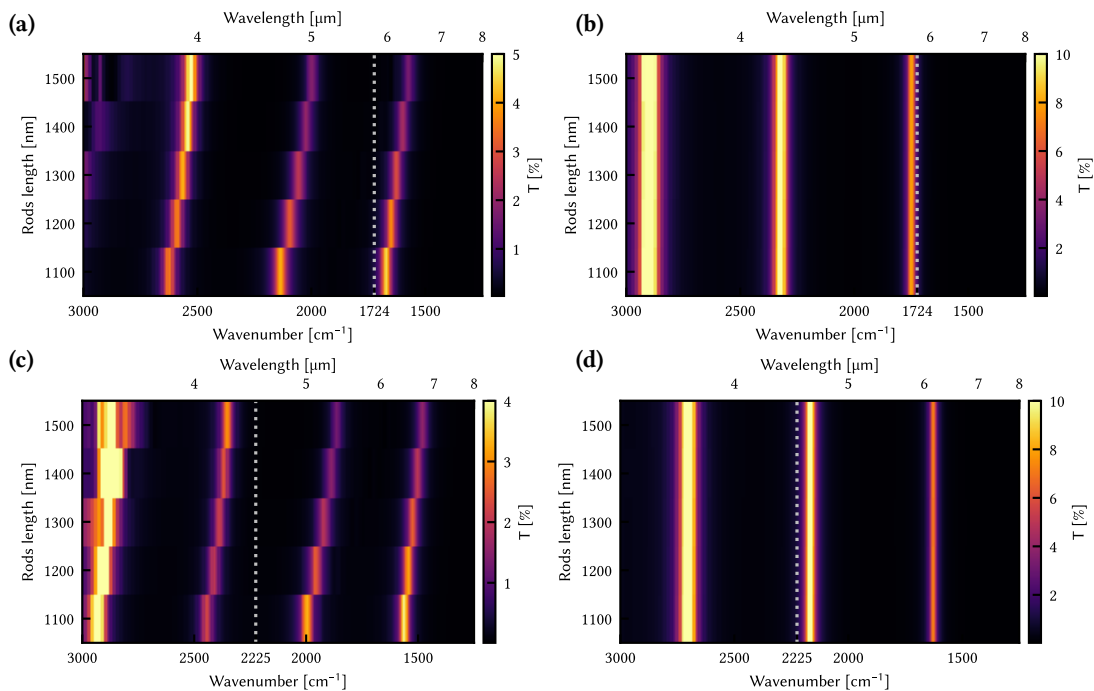


Figure S3. Simulated transmission spectra with the oscillator strength set to zero of: **(a-b)** the coupled rods in the FP cavity with hexanal, with the polarisation along the rods axis and perpendicular, respectively; **(c-d)** the coupled rods in the FP cavity with 4-butylbenzotrile, with the polarisation along the rods axis and perpendicular, respectively.

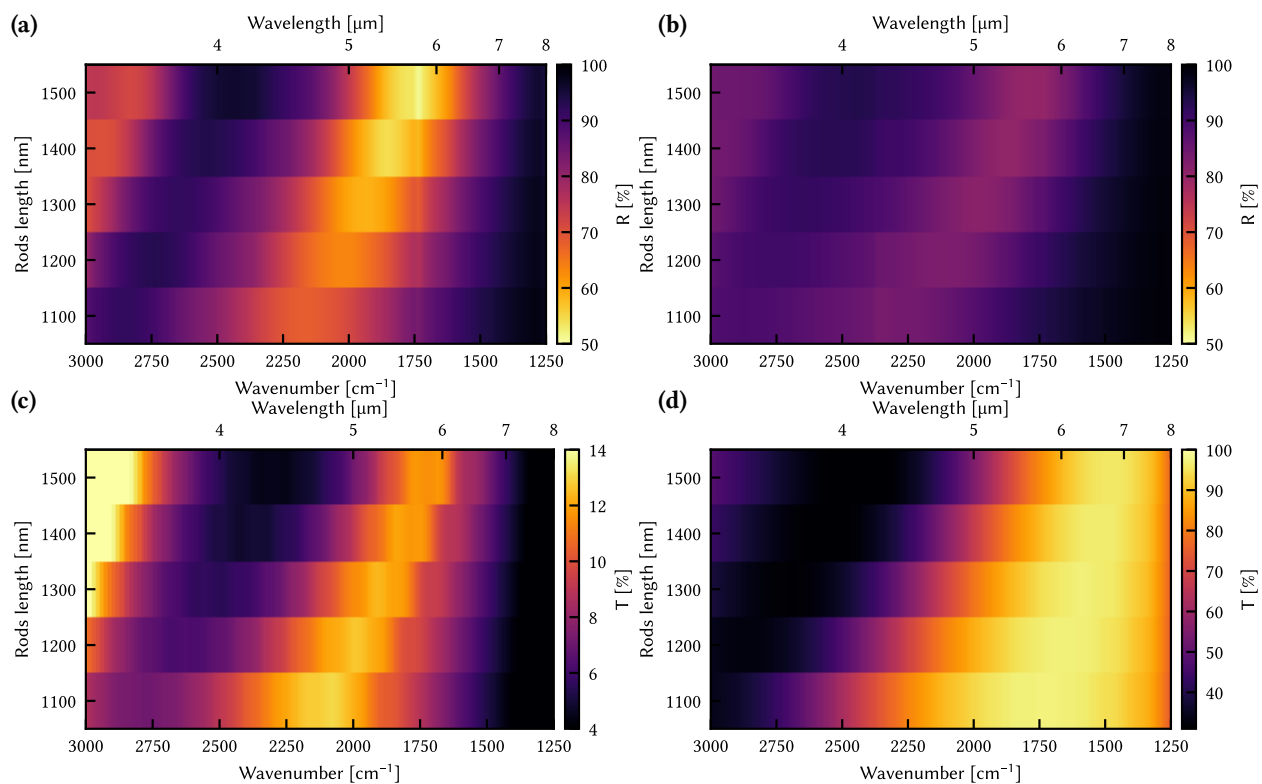


Figure S4. (a)-(b) Reflection map of the gold arrays with the polarizer along and perpendicular to the rods long axis, respectively. (c)-(d) Simulated transmission spectra of the gold arrays with and without a bottom mirror, respectively.

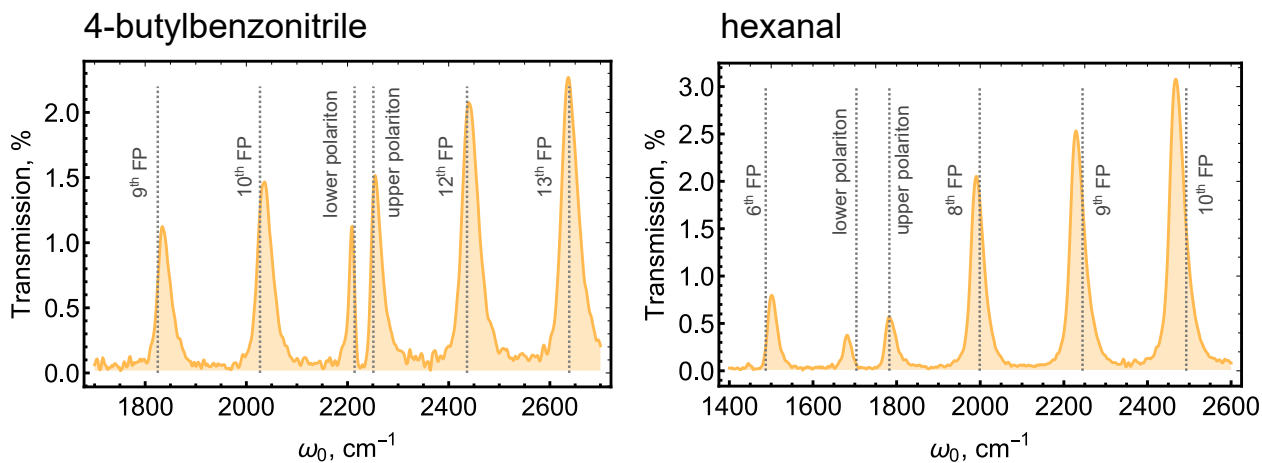


Figure S5. Transmission spectra of filled cavity without the gold nanorods array. The vertical dotted lines represent the fitting of the cavity+molecules systems.

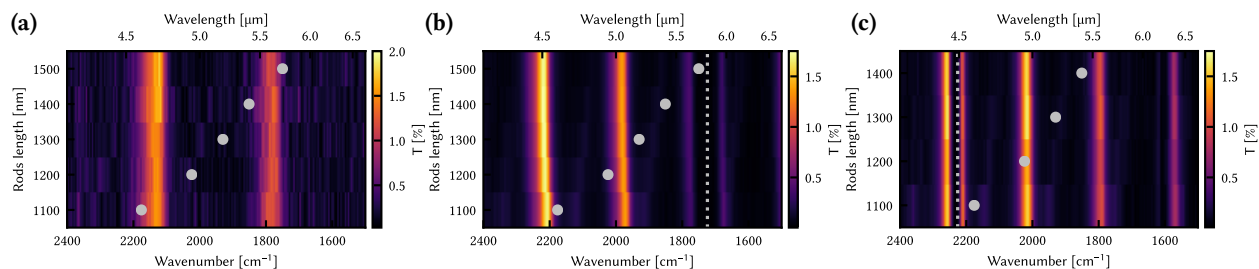


Figure S6. (a)-(c) Transmission maps of the gold nanorods inside the Fabry-Pérot cavity, containing air, hexanal, or 4-butylbenzotrile, respectively. All three were measured with a polarizer perpendicular to the long axis of the rods. The gray dashed line indicates the absorption band of interest of the molecules and the gray dots indicate the plasmon absorption maximum.

Table 2. FWHM of relevant transitions and FP modes. All linewidths are given in cm^{-1} and rod lengths in nm.

media in cavity	air		hexanal	4-butylb	
FP mode FWHM*	84 ± 7.3		42 ± 1.6	31.3 ± 2.9	
Rod length [nm]	1100	1200	1300	1400	1500
Bare plasmon [cm^{-1}]	1120	1032	882	745	621
FP/rods polariton [cm^{-1}]	69.5 ± 0.5	72 ± 6	72.5 ± 0.5	66^\dagger	66^\dagger
FP/rods/hexanal polariton [cm^{-1}]	41.3 ± 7.4	41.3 ± 4.5	40.5 ± 2.5	36.3 ± 4.5	39.5 ± 1.5
FP/rods/4-butylb polariton [cm^{-1}]	34.3 ± 2.9	34 ± 2.8	33.5 ± 1.5	29 ± 4	/

* Measured next to the array

† Too low signal-to-noise to measure more than 1 peak

References

- (1) Johnson, P. B.; Christy, R. W. Optical Constants of the Noble Metals. *Phys. Rev. B* **1972**, *6*, 4370–4379.
- (2) George, J.; Chervy, T.; Shalabney, A.; Devaux, E.; Hiura, H.; Genet, C.; Ebbesen, T. W. Multiple Rabi Splittings under Ultrastrong Vibrational Coupling. *Phys. Rev. Lett.* **2016**, *117*, 153601.